

Large Photothermal Effect in Sub-40 nm h-BN Nanostructures Patterned Via High-Resolution Ion Beam

Josué J. López,* Antonio Ambrosio, Siyuan Dai, Chuong Huynh, David C. Bell, Xiao Lin, Nicholas Rivera, Shengxi Huang, Qiong Ma, Soeren Eyhusen, Ido E. Kaminer, Kenji Watanabe, Takashi Taniguchi, Jing Kong, Dimitri N. Basov, Pablo Jarillo-Herrero, and Marin Soljačić

The controlled nanoscale patterning of 2D materials is a promising approach for engineering the optoelectronic, thermal, and mechanical properties of these materials to achieve novel functionalities and devices. Herein, high-resolution patterning of hexagonal boron nitride (h-BN) is demonstrated via both helium and neon ion beams and an optimal dosage range for both ions that serve as a baseline for insulating 2D materials is identified. Through this nanofabrication approach, a grating with a 35 nm pitch, individual structure sizes down to 20 nm, and additional nanostructures created by patterning crystal step edges are demonstrated. Raman spectroscopy is used to study the defects induced by the ion beam patterning and is correlated to scanning probe microscopy. Photothermal and scanning near-field optical microscopy measure the resulting near-field absorption and scattering of the nanostructures. These measurements reveal a large photothermal expansion of nanostructured h-BN that is dependent on the height to width aspect ratio of the nanostructures. This effect is attributed to the large anisotropy of the thermal expansion coefficients of h-BN and the nanostructuring implemented. The photothermal expansion should be present in other van der Waals materials with large anisotropy and can lead to applications such as nanomechanical switches driven by light.

1. Introduction


The properties of atomically thin 2D materials can be drastically modified at the nanoscale. Thus, significant effort over the past decade has focused on creating nanostructures and nanoscale devices from 2D crystals such as graphene that can manipulate their excellent optoelectronic, thermal, and mechanical properties. There has also been recent work in creating van der Waals (vdW) heterostructures composed of graphene, hexagonal boron nitride (h-BN), and other 2D materials with hybrid properties^[1–3] beyond those that can be achieved using a single type of 2D crystal. For this reason, h-BN has emerged as an invaluable material because it is an ideal substrate for preserving the intrinsic properties of 2D materials and nanotubes.^[4–6] On its own merit, h-BN has become an exciting theoretical and experimental platform to study new regimes of light–matter interactions including highly confined hyperbolic phonon polaritons

J. J. López, Prof. J. Kong
Department of Electrical Engineering and Computer Science
Massachusetts Institute of Technology
Cambridge, MA 02139, USA
E-mail: jjlopez@mit.edu

Dr. A. Ambrosio, Prof. D. C. Bell
Center for Nanoscale Systems
Harvard University
Cambridge, MA 02138, USA

Dr. S. Dai
Department of Physics
University of California
San Diego, La Jolla, CA 92093, USA

C. Huynh, Dr. S. Eyhusen
Carl Zeiss Microscopy
LLC
Peabody, MA 01960, USA

 The ORCID identification number(s) for the author(s) of this article can be found under <https://doi.org/10.1002/sml.201800072>.

DOI: 10.1002/sml.201800072

Dr. X. Lin
Division of Physics and Applied Physics
School of Physical and Mathematical Sciences
Nanyang Technological University
Singapore 637371, Singapore

N. Rivera, Dr. Q. Ma, Dr. I. E. Kaminer, Prof. P. Jarillo-Herrero, Prof. M. Soljačić
Department of Physics
Massachusetts Institute of Technology
Cambridge, MA 02139, USA

Prof. S. Huang
Department of Electrical Engineering
The Pennsylvania State University
University Park, PA 16802, USA

Dr. K. Watanabe, Dr. T. Taniguchi
National Institute for Materials Science
Namiki 1-1, Tsukuba, Ibaraki 305-0044, Japan

Prof. D. N. Basov
Department of Physics
Columbia University
New York, NY 10027, USA

(HPPs),^[7,8] hybridized surface-phonon-plasmon polaritons,^[9–11] subdiffractive focusing, and imaging,^[12–15] and are predicted to cause emitters to preferentially decay via the emission of phonon polariton pairs.^[16] h-BN can also be a tunable single-photon emitter via atom-like defects which can lead to integration in photonic quantum technologies.^[17] Lastly, h-BN nanosheets and flakes have recently been shown to have nonlinear optical properties and temperature-dependent photoluminescence which may be used in multiphoton imaging and quantum photonics.^[18,19] To fully exploit the exciting attributes of h-BN and other vdW materials, we must be able to engineer structures at the meso- and nanoscale. Therefore, it becomes crucial to both push the limits of nanoscale patterning techniques and understand how these methods subsequently modify the properties of 2D materials, such as the absorption and scattering of light and related phenomena.

Recently, neon ion beam lithography has been presented as a method of creating nanostructures beyond the reach of most nanofabrication techniques such as electron-beam lithography^[20] and has been identified as the ideal ion for milling structures at the nanoscale,^[21] yet there is still much progress that can be made when applying these techniques to vdW materials and heterostructures. Previous work that studied the ion beam patterning of 2D materials, has primarily focused on the sputtering of monolayer graphene via a gallium ion beam,^[22] control of defects and electronic doping in encapsulated graphene via a helium ion beam,^[23] nanoscale patterning of monolayer graphene,^[24–27] and nanoscale patterning and electrical-tuning of few-layer molybdenum disulfide (MoS₂).^[28] Recent work has reported the effects of both helium and neon irradiation at 30 keV on monolayer graphene and MoS₂.^[29] However, the sub-50 nm patterning of multi-layer and insulating vdW crystals such as h-BN is even more challenging due to strong charging effects and is yet to be demonstrated. To our knowledge, there have been no studies that provide a comprehensive understanding of both the high-resolution (<50 nm) helium and neon ion beam patterning in any 2D material and how nanostructuring affects light–matter interactions in the material. These aforementioned issues must be studied and resolved if the advantages of direct and high-resolution ion beam patterning are to be implemented for tailoring vdW heterostructures at the nanometer and near atomic-scale.

In this paper, we present high-resolution ion beam patterning of h-BN nanostructures with individual feature sizes down to 20 nm and, equally as important, correlate Raman spectroscopy to near-field scanning probe based spectroscopy and imaging to study coupling with light. Both photothermal and scattering-type scanning near-field optical microscopy (s-SNOM) imaging and spectroscopy^[30–32] were used to understand the influence of nanostructuring on absorption, scattering, and photothermal expansion mediated through the optical phonons in h-BN. We observe a geometry and thickness dependent photothermal expansion of h-BN nanostructures that can be explained via the large anisotropy of the thermal expansion coefficients of h-BN. Specifically, the largest photothermal effect is measured within nanostructures that have the largest height to width aspect ratios. To date, this photothermal expansion in 2D nanostructures has not been reported and can provide great insight into the different ways that nanostructuring can affect the optical

and mechanical properties of h-BN and other 2D materials with anisotropic crystal properties.

2. Results and Discussion

2.1. Ion Beam Patterning

Figure 1 shows the resulting h-BN nanostructures created from a variation in the helium and neon ion dosage. A different h-BN flake was used for each ion dosage test. Multilayer h-BN flakes used in the ion beam patterning process were prepared by the standard exfoliation process^[33] from bulk h-BN crystals. The h-BN flakes were annealed to remove organic contamination before being exposed to either the helium or neon ion beam patterning (see the Experimental Section for details regarding the number of samples and all other characterization techniques). **Figure 1a** is a schematic of the ion bombardment and nanoscale patterning process. The different types of interactions created by energetic ions incident on materials are well known and explained by previous work.^[24] Both the helium (He⁺) and neon (Ne⁺) ion patterning was performed with a Zeiss Orion NanoFab system at the optimal accelerating voltages for high-resolution patterning, 30 and 25 keV respectively. An ion dosage sweep was conducted with a grating pattern with a 30 nm pitch (smaller grating pitches in **Figure S1** in the Supporting Information). Nanoscale patterning in h-BN flakes can be observed by a change in the optical contrast of the exposed regions after patterning, **Figure 1b**. The ion dosages for both helium, **Figure 1c–f**, and neon, **Figure 1g–j**, were varied between 1000 and 40 000 pC cm⁻¹ to determine the optimal dosage for nanoscale patterning. **Figure 1e,f** demonstrates that the helium ion dosage of 20 000 and 40 000 pC cm⁻¹ clearly defined the pattern. **Figure 1g–j** demonstrates that all dosages of the neon ion beam defined the pattern. Notably, neon ion dosages of 1000 and 10 000 pC cm⁻¹ uniformly patterned the surface without introducing undesired surface roughness and undulations. At and above 20 000 pC cm⁻¹, the h-BN surface developed undulations in height due to the increased sputtering and number of secondary interactions created during the recoil of ions within the sample. At these and higher ion dosages, it is likely the beginning of bubble formation due to inert gas being implanted in the sample plays a role in forming the undulations.^[34,35] The dosage ranges for both ions and the qualitative effects can be confirmed by simulating the trajectories of the ion beams within the respective samples.

2.2. Monte Carlo Simulations

To understand the interaction mechanisms between the different bombarded ions and the h-BN, Monte Carlo simulations shown in **Figure 2** were performed using the stopping and range of ions in matter (SRIM) software package.^[36,37] The simulation for helium (**Figure 2a**) shows that the majority of the ions passed through the h-BN with minimal interactions. Therefore, the majority of the ion energy was deposited onto the underlying SiO₂/Si. When compared to helium ions, the neon ions had a greater interaction with the h-BN (**Figure 2b**)

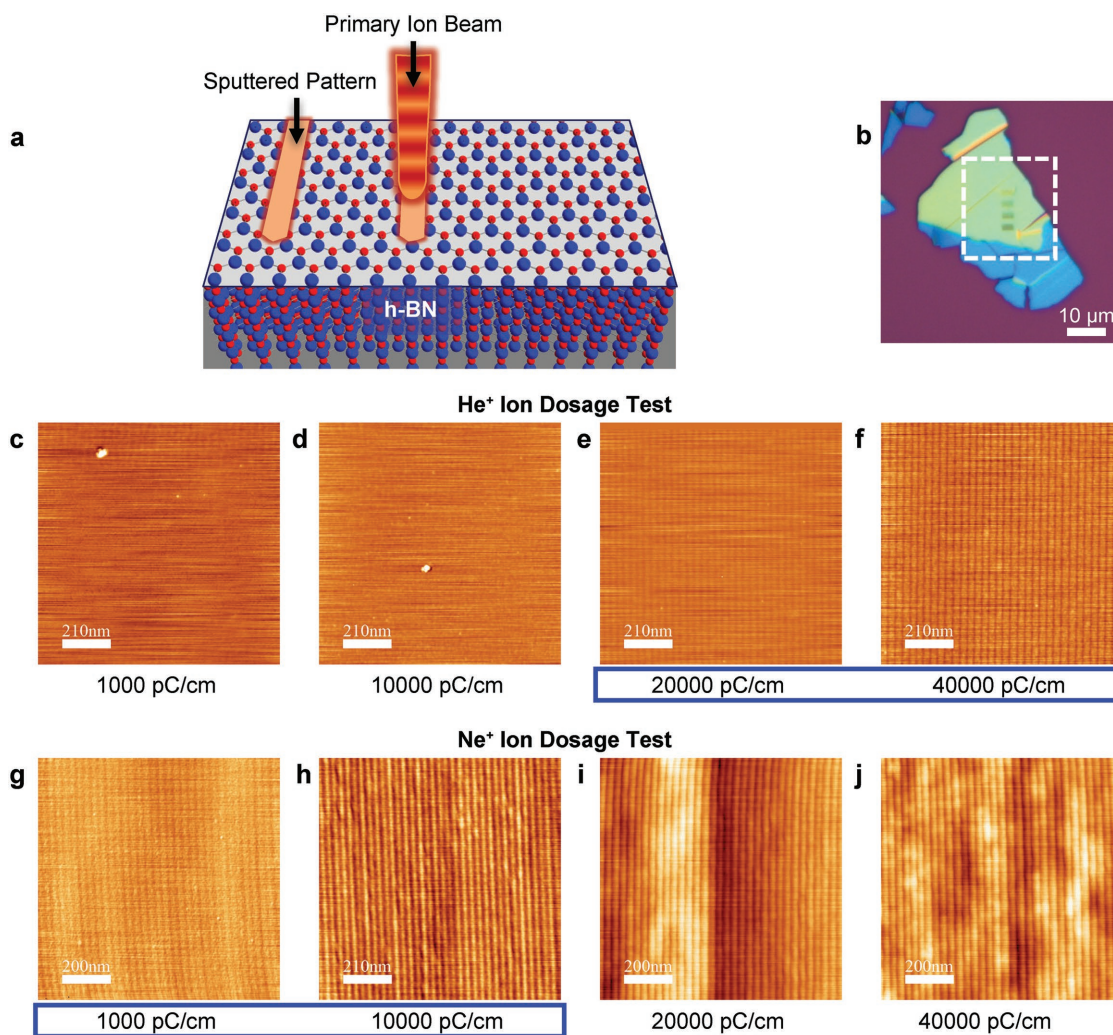


Figure 1. Hexagonal boron nitride (h-BN) ion beam nanopatterning. a) Schematic of ion bombardment and nanoscale patterning. b) Optical micrograph of an example h-BN flake after ion beam patterning (dashed white box contains dosage test area). c–f) Atomic force microscope scans (topography) of helium ion dosages at 30 keV. The array of patterned lines in each dosage test goes from left to right. Each line is etched from top to bottom. The horizontal artifacts in each scan are instrument noise. c) 1000 pC cm⁻¹. d) 10 000 pC cm⁻¹. e) 20 000 pC cm⁻¹. f) 40 000 pC cm⁻¹. The helium dosages between 20 000 and 40 000 pC cm⁻¹ clearly defined the pattern (highlighted with the blue boundary). g–j) Atomic force microscope scans of neon ion dosages at 25 keV. g) 1000 pC cm⁻¹. h) 10 000 pC cm⁻¹. i) 20 000 pC cm⁻¹. j) 40 000 pC cm⁻¹. Neon dosages between 1000 and 10 000 pC cm⁻¹ clearly defined the pattern without undesired surface ripples and roughness (highlighted with the blue boundary).

and therefore transferred a greater amount of ion energy to the h-BN lattice—resulting in a higher sputtering yield. The TRIM simulations confirm the experimental results shown in Figure 1. In Figure 2c,d, the plots of atomic distributions estimate the number of lattice atoms that undergo recoil at each specific target depth. Multiplying the ratio by the ion dose (units of atoms cm⁻²), the ordinate (y-axis) of the plot is converted directly into a density distribution (units of atoms cm⁻³). Even though neon ions have an interaction volume similar to helium ions, their larger mass allows for a greater transfer of energy to the target material via elastic collisions (nuclear energy losses) and thus produce a higher sputtering yield.^[21,38,39] This explains why Monte Carlo simulations predict that the neon ion causes over 10 times more boron and nitrogen ions to undergo recoil within the sample when compared to helium. This is in accordance with the number of ions required to sputter with helium

and neon in the dosage tests performed. Therefore, in terms of high-resolution patterning, neon ions provide the best balance between resolution and sputtering ability. These results can be taken as bench marks when patterning insulating 2D materials and other nonconductive crystalline materials such as diamond which has become an important material for quantum communication applications.

We highlight that future theoretical studies will be required to understand the intricate details of how ion beams interact with h-BN. The transfer of momentum and energy between the incident ion and the target material depends on several factors including: the ion energy, ion mass, target mass, incidence angles of the ion, lattice displacement energy, and additional effects such as crystal orientation and ion channeling.^[39,40] Since the collision cascades that lead to sputtering depend on the ratio of the target and incident ion mass,^[38] the

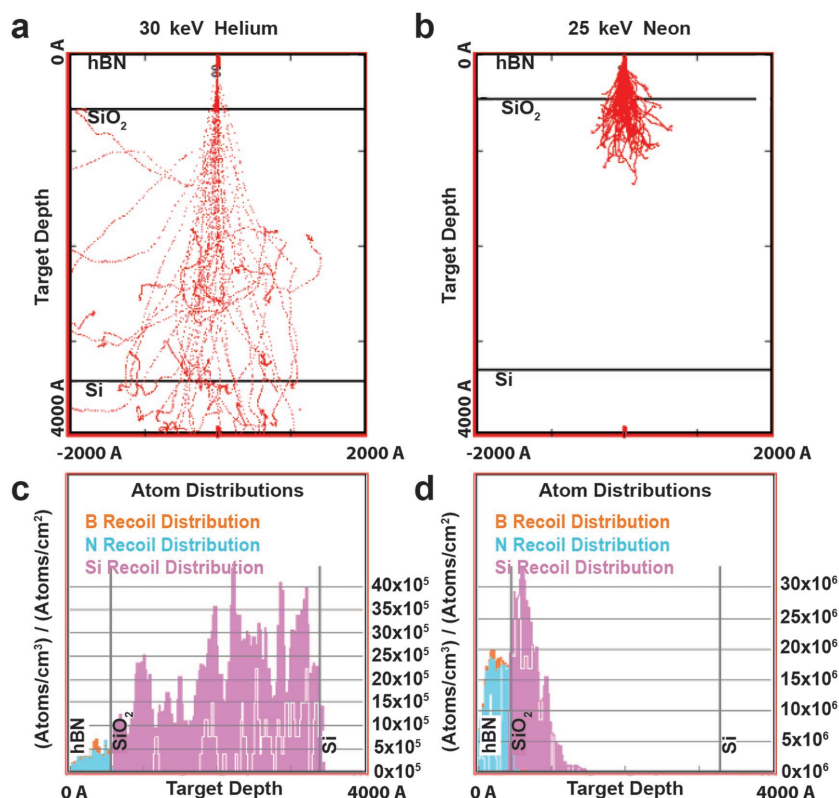


Figure 2. Monte Carlo simulations of ion trajectories. Simulations comparing the range and trajectory of a) 30 keV He⁺ ions in 56.5 nm thick h-BN and b) 25 keV Ne⁺ ions in 45 nm thick h-BN on top of the SiO₂ substrate. c,d) Atomic distributions for each simulation provide the number of ions that undergo recoil at a specific target depth. When comparing the plots, the Ne⁺ ion causes over 10 times more boron and nitrogen ions to undergo recoil throughout the sample which is consistent with the dosage tests performed.

sputtering of boron and nitride should not differ drastically from other elements that are of similar atomic mass. Nevertheless, a unique challenge of patterning h-BN and other electrically insulating materials comes from the accumulation of charge during the milling process which causes potential deflection of the ion beam. Thus, it is important to perform parameter sweeps to understand the optimal dosage for each material (as demonstrated herein). Since the TRIM model simulates the target material as isotropic and amorphous it means that the effects of crystal orientation and channeling effects are not taken into account.^[41] Therefore, atomistic simulations such as molecular dynamics and density functional theory need to be implemented to fully capture the effects of ion irradiation on low-dimensional and multilayered systems such as h-BN. These models have been developed for simple cases of graphene^[42] and will need to be extended to new and emerging 2D materials. Nonetheless, the TRIM model is still used as a standard guideline during experimental studies and confirms the nanopatterning results to first order.

2.3. Atomic Force Microscopy

Once an optimal range for the neon ion dosage was determined, a h-BN grating with a 35 nm pitch was fabricated over a

400 μm² area (with a dosage of 2000 pC cm⁻¹ which is equivalent to 12 ions nm⁻¹, all other neon ion beam parameters were kept the same as in the dosage test). **Figure 3** shows the optical and atomic force microscopy (AFM) images and cross-sections of the 400 μm² patterned area. The difference in optical contrast of the grating is due to a variation in the thickness due to patterning the crystal step edges present in the exposed region. These step edges were present in the thicker portion of the h-BN flake before the ion beam patterning process was performed. The topographical variations in the nanopatterned sample are explained next and the subsequent effects on the optical properties of these h-BN nanostructures are discussed later.

AFM of the pattern was done to understand the exact features milled into the h-BN, **Figure 3b,c**. The AFM in **Figure 3b** shows the bottom right corner of the grating in **Figure 3a**. These scans show crystal step edges in the middle and the bottom of the region which were created due to an uneven mechanical exfoliation process. These step edges allowed us to study the influence of ion bombardment on a range of h-BN thicknesses and topography. A high-resolution AFM scan (using a tetrahedral tip with a 7 nm radius and 7:1 tip aspect ratio) was performed in the thinner region of the grating to reach the bottom of the etched features (**Figure 3c**), see the Experimental Section for more

information. The cross-section in **Figure 3d** demonstrates the overall height profile of the 400 μm² grating. After patterning, the thinner region of the h-BN grating had an average height of 24 nm with a standard deviation (SD) of 1.5 nm, while the thicker region had an average height of 37 nm with a SD of 4.7 nm. The larger SD in the thicker region indicates that the subsequent nanostructures have a more irregular height to width aspect ratio.

In general the ion milling process proceeds as follows: At the beginning of the milling process, the sputtering yield of h-BN should be greater as the ions penetrate the initial side walls of the etched nanostructure due to an increased incident angle.^[38] As the trenches are made deeper, the redeposition of sputtered material in the active milling site increases until the rate of redeposition is equal to the rate of sputtering,^[41] thus self-limiting the etching depth. The AFM shows that the ion beam milling process did reduce the thickness of the h-BN regions exposed to the neon ion beam. This effect is seen by the reduction of the thinner region from 37 to 24 nm. This reduction via milling also occurred in the thicker region of the grating. By observing the heights of the crystal step edges in the nonpatterned regions of h-BN (**Figures 3b** and **5b**), we deduce that the crystal step edges within the thicker region of the grating were flattened out during the milling process. The flattened remnants of the crystal step edges can be clearly seen in **Figure 3b**

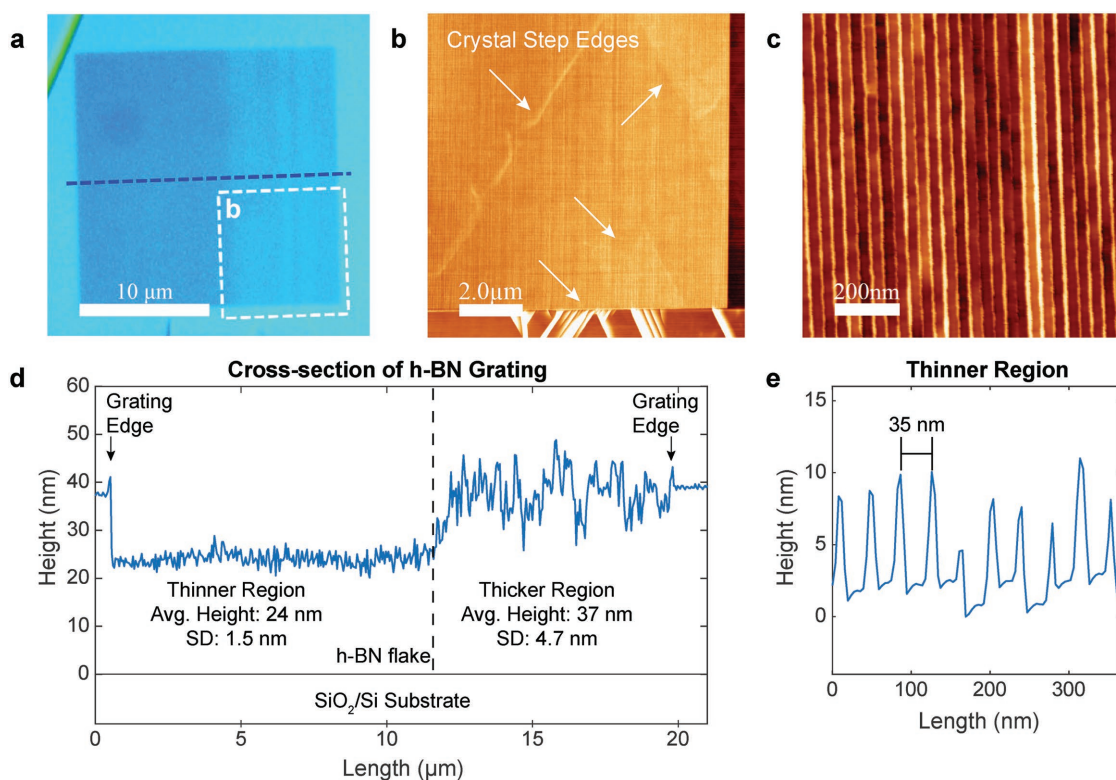


Figure 3. h-BN grating with optimal neon dosage. a) Optical micrograph of a $400 \mu\text{m}^2$ h-BN grating fabricated via neon ion beam patterning at 25 keV. The difference in optical contrast is due to a gradient in height which was created by patterning the crystal step edges found in the exposed region. b,c) AFM scans of the h-BN grating. There are two distinct regions in the grating with different average thicknesses and standard deviations measured for the nanostructure heights. b) $100 \mu\text{m}^2$ scan of bottom right corner in Figure 3a denoted by the white dashed box (scanned with a standard AFM tip radius of 10 nm). c) $1 \mu\text{m}^2$ scan of the milled pattern in the thinner region of the grating (scanned with a high-resolution AFM tip radius of 7 nm). d) Cross-section of the entire grating which is represented by the blue dashed line in (a). e) Cross-section of the $1 \mu\text{m}^2$ scan in the thinner region confirming a pitch of 35 nm, a mill depth between 6 and 8 nm, and a nanostructure width of ≈ 20 nm.

indicated by multiple arrows. The larger variation in nanostructure height within the thicker half of the h-BN was due to these crystal step edges being directly exposed to the neon ion beam. The exposed edges provided a jagged template leading to sharp variations in height after patterning, leading to nanostructures with larger aspect ratios. Even though the surface was not ideal in the thicker region, the 35 nm pitch pattern is also detected in the first few nanometers of the thicker region. Zoomed-in AFM in Figure S5 (Supporting Information) demarks the pattern on the top h-BN layers. This contrasts with the uniform etch depth on the thinner half of the grating. Figure 3e shows the cross-section of a high-resolution AFM in the uniformly patterned section of the grating (thinner region). Topography shown in Figure 5b demonstrates that there were no crystal step edges in the thinner half of the grating. The semiflat region at the bottom of each nanostructure profile confirms that the high-resolution AFM tip reached the bottom of each etched feature. It further demonstrates that the smallest nanostructures etched were between 6–8 nm deep and ≈ 20 nm wide.

2.4. Raman Spectroscopy

To understand the effects of the nanopatterning on the crystal structure of h-BN, Raman spectroscopy with a laser spot size of

$1.30 \mu\text{m}$ was used to observe the optically active phonons and any subsequent disorder introduced at the nanoscale, including dislocations and amorphization of the h-BN crystal (via vacancies) as previously seen in crystalline materials.^[35,43] Previous Raman spectroscopy of h-BN has demonstrated a characteristic peak for the E_{2g} in-plane optical phonon mode^[44–46] at 1366 cm^{-1} . Figure 4 demonstrates the corresponding Raman spectra and maps that identify vibrational modes in the sample. Figure 4a shows the Raman spectrum measured from three different regions: the nonpatterned h-BN (≈ 40 nm in height), thinner grating region (≈ 24 nm in height), and thicker grating region (≈ 37 nm in height). Zoomed-in spectra of the thinner and thicker regions are shown in Figure 4b demonstrating that the h-BN peak at 1366 cm^{-1} is twice as strong in the thicker region compared to the thinner region which is reasonable due to the difference in thickness. Figure 4c,d shows the Raman maps with the value of the integrated area under each corresponding peak within the ranges $1335\text{--}1395$ and $1420\text{--}1480 \text{ cm}^{-1}$. As seen from the Raman spectrum and map, the h-BN phonon peak at 1366 cm^{-1} was sharp and unmodified in the nonpatterned region of h-BN and decreased significantly as the Raman scan moved from the edge of the pattern and into the grating. When compared to the nonpatterned h-BN in location 3 in Figure 4c there was a ≈ 49 times reduction of the Raman intensity in the thicker region and ≈ 234 times reduction in the thinner region.

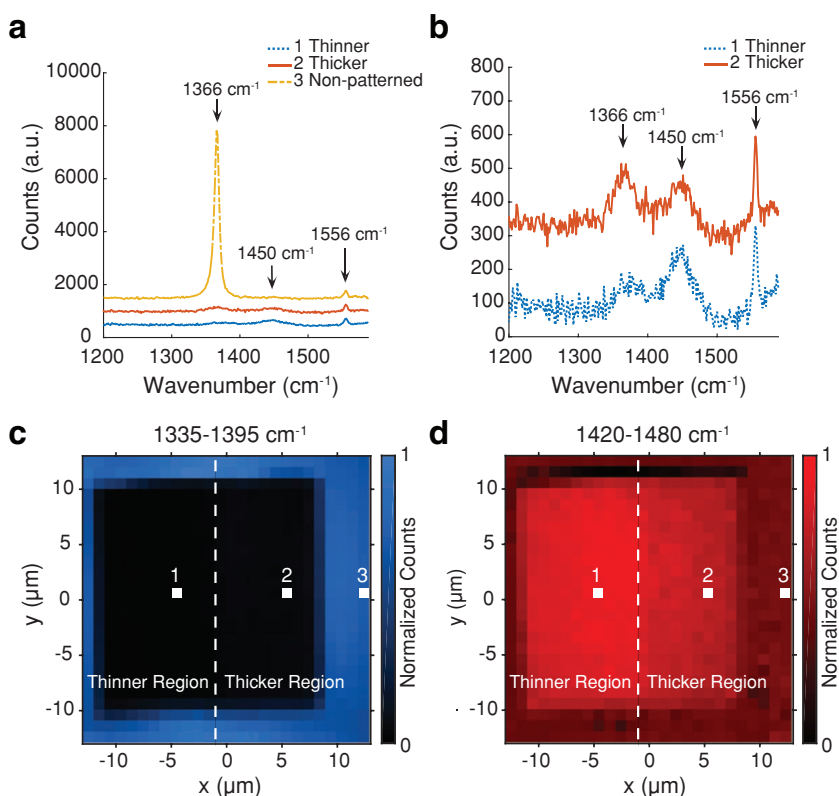


Figure 4. Raman spectroscopy and Raman maps. a) Raman spectrum comparing three regions of the sample: thinner region, thicker region, and nonpatterned. The corresponding positions for spectra 1–3 are labeled on the Raman maps in (c) and (d). The peaks identified are the h-BN optical phonon mode at 1366 cm^{-1} , third order silicon TO phonon at 1450 cm^{-1} , and ambient oxygen at 1556 cm^{-1} . b) Plot comparing the Raman spectra inside the thinner and thicker region of the grating. c,d) Raman maps showing the value of the integrated area under the peaks found within the ranges $1335\text{--}1395$ and $1420\text{--}1480\text{ cm}^{-1}$. All maps are normalized to the maximum counts found within each wavenumber range. c) Intensity map of the h-BN phonon peak found within $1335\text{--}1395\text{ cm}^{-1}$. d) Intensity map of the silicon TO phonon peak found within $1420\text{--}1480\text{ cm}^{-1}$.

Similar ratios hold regardless of what exact location is used for the nonpatterned reference. The Raman peak of the third order silicon transverse optical (TO) phonon^[47,48] at 1450 cm^{-1} grew stronger in intensity as the scan moved from the pattern edge and into the grating as seen in Figure 4d. Moreover, the signal of the silicon TO phonon (underneath the h-BN) was stronger in the thinner region compared to the thicker region. The signal from the silicon phonon was most likely strongest in the areas where the ion milling of the h-BN made the flake thinner and allowed the laser to couple to the silicon underneath the nanostructured h-BN, thus providing a stronger Raman signal intensity. Lastly, we note the Raman peak at 1556 cm^{-1} is not location dependent and is most likely due to ambient oxygen as recently reported for related experiments.^[49]

There are at least three possible reasons for the reduction of the Raman signal for the h-BN phonon at 1366 cm^{-1} . The first is a reduction normally indicates surface and boundary defects that affect the phonons. Second, Ne^+ ion interstitials within the plane or between the h-BN layers could further modify the vibrational modes. These conclusions are supported since recent work has shown that exposure of supported graphene to

a helium and neon ion beam broadens and reduces the intensity of the E_{2g} phonon mode due to increased disorder.^[29] Although h-BN consists of two different atoms and layered stacks, we expect that these previous results on a similar E_{2g} phonon mode inform our measured reduction of the Raman peak in h-BN. Since ion beam irradiation is known to introduce vacancies, interstitials (Frenkel defects), and amorphization of crystalline materials,^[39,41] these defects are expected to be responsible for the reduction in the intensity of the E_{2g} mode. Lastly, the weaker Raman signal could be from a reduced coupling efficiency of the Raman laser into the sample due to increased light scattering from the nanostructures. Since this is a far-field measurement, the information obtained about the h-BN structures (and phonons) at the nanoscale could be limited; therefore, it is illuminating to use nanoimaging and spectroscopy techniques that provide complimentary and necessary information about the way these materials are engineered at the nanoscale before they can be used in any type of engineered vdW heterostructures and devices.

2.5. Photothermal Spectroscopy and Imaging

To better understand how the nanoscale patterning affected the absorption of light and the coupling to the phonons in h-BN, photothermal spectroscopy and imaging were performed using an Anasys nanoIR2-S system. We show a schematic of the experiment and the resulting photothermal spectroscopy and imaging in Figure 5. The h-BN sample is illuminated with pulsed infrared light with a 1 kHz repetition rate and a frequency, ω_{OPO} , from an optical parametric oscillator (OPO) which is focused on the sample by a low numerical aperture (NA) parabolic mirror. A gold-coated AFM tip in contact mode is used to increase near-field coupling and subsequently detect the local thermal expansion of the sample caused by the absorption of the incident infrared light. According to the photothermal detection scheme,^[50] the mechanical expansion of the sample (due to local heating after light absorption) excites the mechanical resonances of the AFM cantilever (while the AFM tip is in contact mode with the sample) and the measured amplitude of oscillation is proportional to the sample absorption. In this experiment, the two distinct absorption peaks correspond to the excitation of phonons in both the h-BN and the SiO_2 underneath and subsequently provide a chemical signature at the nanoscale. Figure 5c,d shows the IR spectrum taken from various points in both the thinner and thicker regions of the h-BN grating respectively (cross-section shown in Figure 3d). Figure 5c shows an absorption peak for the optical phonon of the SiO_2 ^[50,51] at 1084 cm^{-1} only inside the thinner region and is

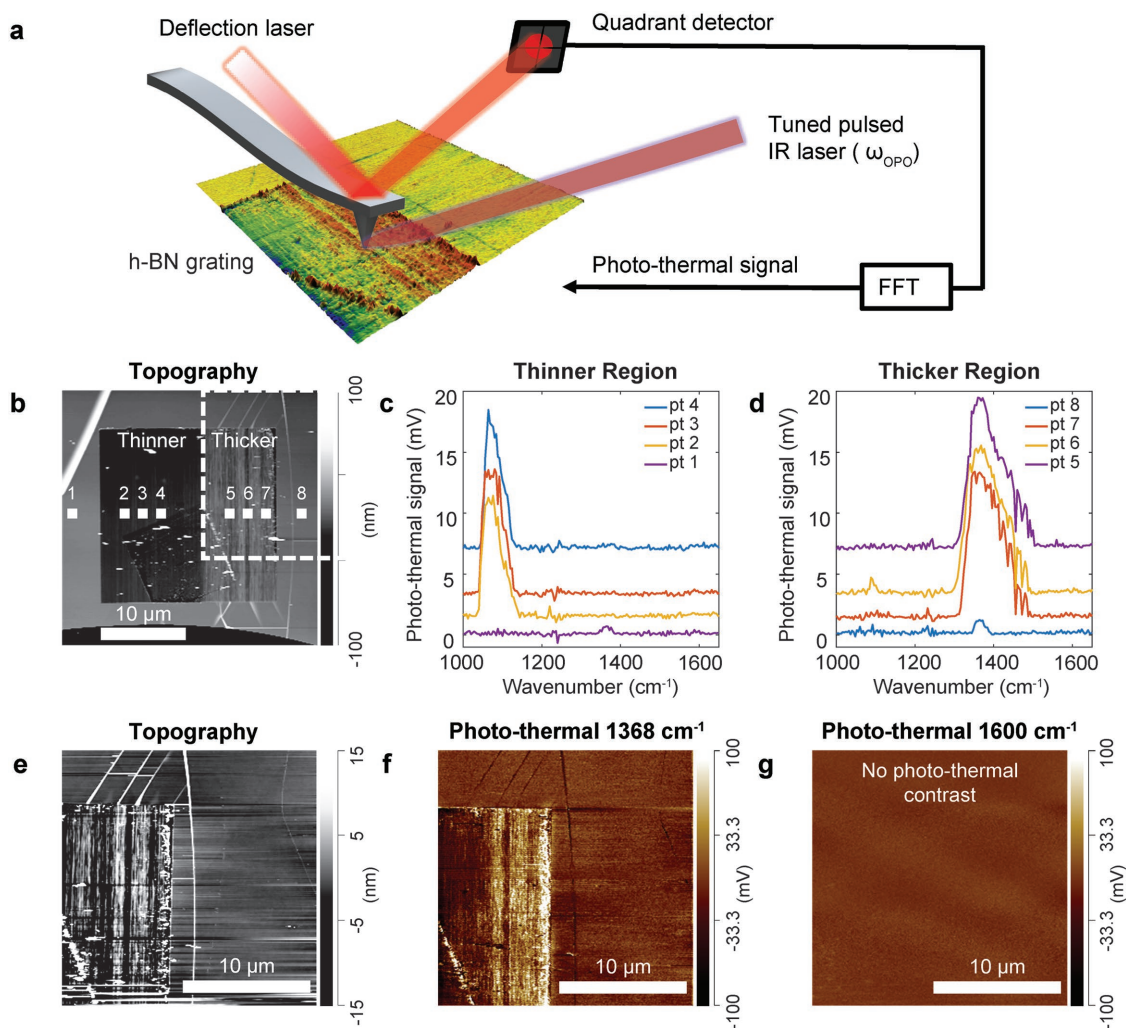


Figure 5. Photothermal infrared spectroscopy and imaging. a) Schematic of the photothermal illumination/detection system. b) AFM image with the location of photothermal (absorption) spectra taken. c) Photothermal spectra taken from four different locations along the thinner region of the h-BN grating, showing a strong SiO₂ absorption peak at $\approx 1084\text{ cm}^{-1}$. d) Photothermal spectra taken from four different locations along the thicker region of the h-BN grating, showing a strong and broad h-BN absorption peak at $\approx 1368\text{ cm}^{-1}$. e) AFM image of the top right corner of the h-BN grating indicated by the white dashed box in (b). f) Photothermal image of the top right corner at $\approx 1368\text{ cm}^{-1}$. g) Photothermal image of the same region at 1600 cm^{-1} . No photothermal contrast was detected, indicating no absorption or mechanical expansion.

not observed either in the thicker region or in the nonpatterned regions of the h-BN (see Figure S6 in the Supporting Information for multiple photothermal line scans). This peak arises because the removal of the top h-BN layers during the ion milling provided increased coupling to the SiO₂ underneath. In Figure 5d, a strong and broad absorption peak at 1368 cm^{-1} corresponding to the TO phonon in h-BN is measured for all points inside the thicker region of the grating—we note that this region has a greater number of layers and has nanostructures with larger aspect ratios (which can be seen from the larger SD of 4.5 nm). The point-to-point spectroscopic differences within the h-BN grating were suggested in the Raman spectra, but the differences in the photothermal spectrum were more substantial and clear with the near-field technique.

Direct photothermal imaging was conducted for the top right of the grating (located in the thicker region), topography shown in Figure 5e. Figure 5f,g demonstrates the photothermal images

collected by scanning the tip while illuminating the sample with one specific wavelength of light. The respective wavenumbers (wavelengths) chosen in Figure 5f,g were 1368 cm^{-1} (on resonance) and 1600 cm^{-1} (off resonance). The photothermal image at 1368 cm^{-1} shows a clear and strong absorption peak at the h-BN phonon mode. This indicates that the photothermal technique can excite and couple to the phonons in the lattice and subsequently measure the mechanical expansion of the nanostructured h-BN due to the absorption of light.

Although the Raman signal for the h-BN phonon mode at 1368 cm^{-1} inside the thicker region is reduced by an order of magnitude (≈ 49 times smaller), the photothermal response inside point 5 of the grating is increased by an order of magnitude (≈ 11 times larger) when compared to the nonpatterned h-BN in point 8, Figure 5b–d. These measured ratios are consistently within the same order of magnitude regardless of the points chosen. Normally a weak Raman signal depicts

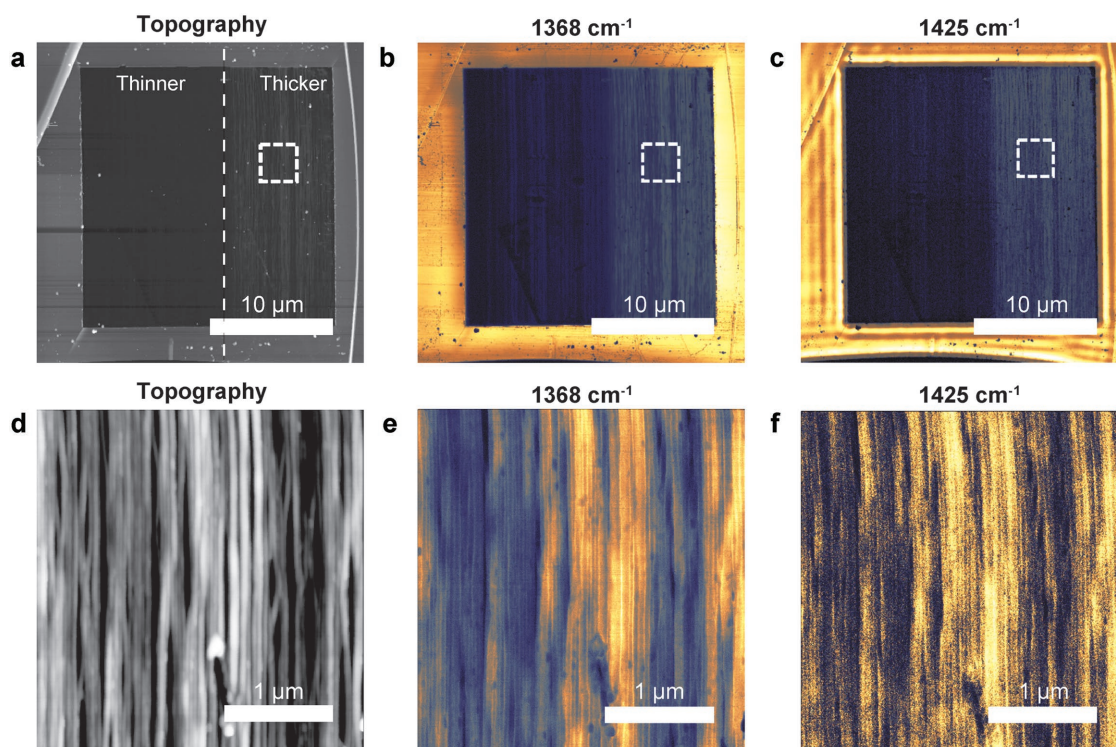


Figure 6. Scattering-type scanning near-field optical microscopy (s-SNOM). a) $28 \times 28 \mu\text{m}^2$ topography scan taken of the entire grating structure. b) s-SNOM image taken at 1368 cm^{-1} . The thicker region of the grating scatters more light than the thinner region. c) s-SNOM image taken at 1425 cm^{-1} . Propagating hyperbolic phonon polaritons are seen in the nonpatterned regions of the sample. d) $9 \mu\text{m}^2$ topography scan, region highlighted by the white box in (a). e) $9 \mu\text{m}^2$ s-SNOM image taken at 1368 cm^{-1} . f) $9 \mu\text{m}^2$ s-SNOM image taken at 1425 cm^{-1} .

substantial defects and strong disorder in a 2D crystalline lattice (as frequently observed in graphene^[52,53]). However, in this case, even though the Raman signal inside the grating is very weak, the photothermal measurement shows strong absorption at the phonon resonance which suggests that the lattice is not completely disordered by the ion beam nanostructuring. Moreover, it is possible that the h-BN layers beneath the top few nanometers of the flake were protected from the ion milling process and obtained minimal damage as suggested previously for encapsulated graphene.^[23]

By examining the topography of the grating, we conclude that the above seemingly contradictory measurements were the result of: i) There was stronger near-field coupling due to the nanopatterning of the surface that produced sharp edges in each nanostructure that strongly interacted with the AFM tip in the photothermal measurement. This interaction then transferred more energy to the phonon modes of the h-BN nanostructures and any unperturbed h-BN layers beneath the surface. ii) The larger height to width aspect ratio of the h-BN nanostructures in the thicker region allowed a larger thermal expansion out of plane. Elaborating on the second mechanism above: it is possible the nanostructuring localized the phonons and subsequently increased heating in the h-BN nanostructures leading to enhanced mechanical expansion. This can be explained because the extreme anisotropy of the h-BN lattice, which contributes to its hyperbolic optical properties,^[12] also results in a drastic difference between the thermal expansion coefficient in the *a*-direction (basal plane) and the *c*-direction

(orthogonal to the basal plane). Specifically, h-BN has a large and positive thermal expansion coefficient of $38 \times 10^{-6} \text{ K}^{-1}$ in the *c*-direction^[54] (as opposed to the small and negative coefficient $-2.7 \times 10^{-6} \text{ K}^{-1}$ in the *a*-direction). Originally emphasized by Lifshits, the increased absorption of light (and subsequent heating) in this highly anisotropic crystal leads to acoustic “bending” waves^[55] which cause the significant expansion in the *c*-direction and contraction in the *a*-direction. This mechanism has been theoretically and experimentally investigated for other bulk layered crystals such as GaS, GaSe, and InSe.^[56] Moreover, the sputtering of the nanoscale lines (and thus the elimination of covalent bonds between adjacent boron and nitrogen atoms) in the basal plane likely allowed the crystal to contract further in the *a*-direction and forced the nanostructure to preserve its volume by expanding in the *c*-direction, contributing to the large photothermal effect.

2.6. Scattering-Type Scanning Near-field Optical Microscopy

Since the photothermal technique has only recently been used to study atomically thin vdW materials, we employed the use of a complimentary technique to ensure that abnormal tip interactions were ruled out as the main reason for the observed large absorption values. Infrared nanoimaging was conducted using a Neaspec s-SNOM. **Figure 6** contains the measurements taken of the entire h-BN grating and of smaller regions at 1368 cm^{-1} and 1425 cm^{-1} respectively to understand how the phonon

vibrations and any possible HPPs supported by the sample were modified by the nanopatterning. Figure 6a depicts the AFM of the entire h-BN grating. The respective s-SNOM (scattering amplitude) images in Figure 6b,c show a stronger scattered signal from the nanostructures in the thicker region (similar to the stronger absorption signal from the photothermal measurement in Figure 5). Figure 6d–f demonstrate topographic and s-SNOM images of the $9 \mu\text{m}^2$ area in the respective white dashed boxes in Figure 6a–c. For both sets of s-SNOM measurements, the AFM tip clearly distinguished the topography of the patterned h-BN while collecting a stronger scattering amplitude from the areas that had large height to width aspect ratios. The difference in measured scattering amplitudes within the grating may be partially due to the difference in the number of h-BN layers underneath each measured point. Furthermore, for the measurements in Figure 6d–f, it is possible that the standard tip used for the s-SNOM was too large to fully interact with the bottom of each individual nanostructure. In spite of the above details, the stronger scattering signal from the thicker region of the grating cannot be solely attributed to poor tip interactions because this area of the sample also has the etched grating “on top” as shown in the Supporting Information. Since both the photothermal and s-SNOM measured stronger signals from the thicker region of the grating, it is concluded that the measured photothermal expansion is not erroneous and was attributed to the nanostructuring.

Lastly, the observation of propagating phonon polaritons in the nonpatterned region of the sample confirms the high quality of the original h-BN flakes and rules out any contamination or unintentional surface modification as causing the increased absorption or scattering signal from the grating. Propagating phonon polaritons in the nonpatterned regions are clearly seen at 1425 cm^{-1} as previously demonstrated in other work.^[7] These HPPs were not observed with the photothermal microscope (Figure 5) due to the lower signal strength of the illumination/detection technique. Interestingly, Li et al.^[57] very recently demonstrated concave wavefronts of a diverging polariton beam in a h-BN grating structure with a 100 nm pitch. Although the thicker region of the h-BN grating in this work did have a stronger scattering amplitude, the s-SNOM technique did not conclusively demonstrate HPPs propagating within the patterned grating region. Thus, we can only speculate that the protected layers underneath the pattern or the grating itself can sustain HPPs, but that would require a systematic study of nanostructure geometry, grating pitch, and h-BN thickness that is beyond the intent of this study. Further studies can pursue the direct connection between the photothermal expansion and phonon polaritons in these types of high-resolution nanostructures. Finally, it should be of great interest that this large photothermal expansion property should be experimentally verifiable in 2D crystals of gallium sulfide (GaS), gallium selenide (GaSe), and indium selenide (InSe) which have only been very recently explored.^[58,59]

3. Conclusion

In summary, we for the first time demonstrated that high-resolution (< 50 nm) ion beam patterning of insulating multilayer

vdW materials (in this case h-BN) is possible and provides a way of modifying the properties of 2D materials at the nanoscale. We show that Ne^+ is a better candidate than He^+ for direct high-resolution patterning of vdW materials. Although Raman spectroscopy of the nanostructured h-BN provides information of defects and the active phonons, it cannot completely elucidate the full optical response and properties of nanostructured materials. For this reason, we used photothermal spectroscopy and imaging on a nanopatterned crystalline vdW material and demonstrated a large photothermal response that was dependent on the height to width aspect ratio of nanostructures. The role of extreme anisotropies and expansion coefficients with opposite signs provides physical intuition for the enhanced photothermal effect. This work provides a baseline for the continued exploration of nanoscale patterning of vdW materials with ion beams. It also shows that correlated far-field and near-field characterization techniques will be especially important as vdW heterostructures are explored and engineered with nanoscale precision.

4. Experimental Section

Number of Samples: A total of four different h-BN flakes for this publication were used: For one helium and one neon ion sample, four different dosages (1000, 10 000, 20 000, and 40 000 pC cm^{-1}) were performed. For the helium ion sample found in the Supporting Information, 4 different pitches (30, 20, 10, and 5 nm) were performed. Lastly, one large-area $400 \mu\text{m}^2$ sample was performed at $2 000 \text{ pC cm}^{-1}$ with neon which was studied via both Raman spectroscopy and scanning probe microscopy. Additionally, this study chose to focus on a single large-area sample for multicharacterization because to the authors' knowledge no publication to date on 2D material nanopatterning has presented a complete end-to-end study using several characterization techniques to confirm light–matter interaction effects after ion beam nanopatterning. The neon ion beam patterning process was not the limiting factor since it took ≈ 1 h to complete the $400 \mu\text{m}^2$ grating. In this case, each large area scan with Raman, high-resolution AFM, photothermal, and s-SNOM required long acquisition times (8–12 h) and several sessions to take reliable data with high enough resolution.

Sample Preparation: Silicon wafers with a 285 nm thick thermal oxide were used as substrates for all samples. The substrates were cleaned with O_2 plasma using a Plasma-Preen system (Plasmatic Systems, Inc.) for 30 s before any h-BN flakes were mechanically exfoliated onto the substrate. The h-BN flakes were exfoliated from bulk samples synthesized under high pressure as previously reported by Watanabe et al. After exfoliation, the samples were annealed in 1:1 ratio O_2/Ar mixture at $500 \text{ }^\circ\text{C}$ for 4 h to remove organic contamination remaining from the exfoliation process. To avoid organic contamination from ambient air, samples were cleaned with O_2 plasma at 30 W for 30 s immediately before they were placed in the ORION NanoFab. We note that without the last O_2 plasma cleaning step, carbon deposition was seen on other samples where the exposed region of the h-BN crystal was patterned with either helium or neon ions.

Helium and Neon Ion Patterning: Ion beam patterning was performed at the Carl Zeiss Ion Microscopy Innovation Center using a commercial ORION NanoFab system. An ion dosage sweep was conducted with a computer-generated grating pattern. The helium ion beam patterning was done at 30 keV using a 5 mm working distance, 5 μm aperture, spot size of 4.10, and a beam current of 1 pA. The grating patterns were written using a single line using a 0.5 nm pixel. The dosage was varied from 1000 to 40 000 pC cm^{-1} and the pitch was varied from 30 to 5 nm (smaller pitches in Figure S1 of the Supporting Information).

The neon ion beam patterning was done at 25 keV using a 5 mm working distance, 10 μm aperture, spot size of 4.00, and a beam current of 1 pA. The grating patterns were written using a single line using a 0.5 nm pixel. The dosage was varied from 1000 to 40 000 pC cm^{-1} and the pitch was varied between 30 and 35 nm depending on the specific pattern.

Monte Carlo Simulations of Ion Beam Interaction: The ion beam interactions with the sample were calculated with 100 simulated ions using the SRIM software package (<http://www.srim.org/>). The helium ion case was calculated using the following structure schematic: 56.5 nm of h-BN (top), 285 nm SiO_2 (middle), and Si substrate (bottom). The neon ion case was calculated using the following structure schematic: 45 nm of h-BN (top), 285 nm SiO_2 (middle), and Si substrate (bottom).

Atomic Force Microscopy: Initial atomic force microscopy was done with a Veeco Dimension 3100 AFM and BudgetSensors TAP300AL-G-10 Silicon AFM probe with a 10 nm tip radius. Secondary verification of the pitch and mill depth of the 400 μm^2 h-BN grating was done with a Nanosensors SSS-FMR AFM probe with a 5 nm tip radius in the Veeco 3100 and an Olympus AC240BSA-R3 probe with a 7 nm tip radius and 7:1 tip aspect ratio in an Asylum Research Cypher S. The gratings were scanned in the direction perpendicular to the patterned lines. It was highlighted that the high-resolution tips were necessary to reach the bottom of the etched features. Analysis was done with WSXM^[60] freeware.

Raman Spectroscopy: Raman spectroscopy was done using a HoribaLab Raman system operating at room temperature with a 532 nm laser working at 100% power (≈ 50 mW) with an Olympus long working distance 50 \times objective (0.50 NA), 1800 gr mm^{-1} grating, and a 500 μm pin hole. The 26 \times 26 point Raman map was done with a 1 μm point-to-point pixel distance, 2 accumulations per point to reduce noise, and a 30 s acquisition time per point. The laser spot size through the microscope objective was calculated as $1.22 \lambda/\text{NA} = 1.30 \mu\text{m}$.

Photo-thermal Spectroscopy and Imaging: Near field photothermal (absorption) measurements were conducted using an Anasys nanoIR2-S. The optical parametric oscillator has a 10 ns pulse width and a 1 kHz fixed repetition rate. It is estimated that the system never exceeds an illumination power of 175 μW at the sample. The illuminated sample area could be estimated to be tens of micrometers in diameter since the light was focused on the sample by a low NA parabolic mirror at 70° from the vertical. Therefore, it was not expected to have enough power to measure any nonlinear optical properties. The amplitude of the induced mechanical oscillations on the AFM cantilever was monitored at 170 kHz (with a bandwidth of 50 kHz). The oscillations of the cantilever (and subsequent ring down) were analyzed by a fast Fourier transform to obtain all frequencies of oscillation. The photothermal spectrums were collected within the range of 900–2000 cm^{-1} with a resolution of 4 cm^{-1} .

Scattering-Type Scanning Near-field Optical Microscopy: The infrared nanoimaging experiments described in the main text were performed using a scattering-type s-SNOM. The s-SNOM is a commercial system (www.neaspec.com) based on a tapping-mode AFM. In the experiments, a commercial AFM tip (tip radius ≈ 10 nm) with a PtIr coating was used. The AFM tip was illuminated by monochromatic quantum cascade lasers (www.daylightsolutions.com), covering a frequency range of 900–2400 cm^{-1} in the midinfrared. The s-SNOM nanoimages were recorded by a pseudoheterodyne interferometric detection module with an AFM tapping frequency of 270 kHz and tapping amplitude around 70 nm. To subtract the background signal, the s-SNOM output signal was demodulated at the third harmonic of the tip tapping frequency.

Supporting Information

Supporting Information is available from the Wiley Online Library or from the author.

Acknowledgements

While preparing this manuscript, the authors became aware of one work studying the effects of both He⁺ and Ne⁺ irradiation at 30 keV on monolayer graphene and MoS₂.^[29] After submission, that authors became aware of Li et al.^[57] demonstrating concave wavefronts in a h-BN grating. The authors thank all the following insightful discussions and assistance: Prof. Karl Berggren, Dr. Joel Wang, and Aviram Massuda for discussions on nanofabrication, vdW sample preparation, and AFM. Dr. William Wilson and Dr. Farnaz Niroui for discussions regarding the photothermal measurements. Dr. Arthur McClelland and Dr. Steve Kooi for assistance with the Raman Spectroscopy. The Organic and Nanostructured Electronics (ONE) Lab at MIT for access to the O₂ plasma cleaner. Growth of h-BN crystals was supported by the Elemental Strategy Initiative conducted by the MEXT, Japan, and JSPS KAKENHI Grant Numbers JP15K21722 and JP25106006. Exfoliation and annealing of the h-BN samples, optical characterization, and other work by the P.J.-H. group was partly supported by the Center for Excitonics, an Energy Frontier Research Center funded by the US Department of Energy (DOE), Office of Science, Office of Basic Energy Sciences under Award Number DESC0001088 (fabrication) and partly through AFOSR grant FA9550-16-1-0382 (analysis). Analysis by J.J.L. was supported in part by the National Science Foundation (NSF) Graduate Research Fellowship Program (GRFP) under award no. 1122374 and by a MRSEC Program of the NSF under award no. DMR-1419807. X.L. was supported by Chinese Scholarship Council (CSC No. 201506320075). I.K. was partially supported by the Seventh Framework Programme of the European Research Council (FP7-Marie Curie IOF) under Grant No. 328853-MC-BSiCS. Analysis by S.H., J.K., and M.S. was supported by the U.S. Army Research Office through the MIT Institute for Soldier Nanotechnologies (ISN), under award no. 023674. The photothermal microscopy and the majority of the high-resolution AFM and Raman Spectroscopy were performed at the Harvard University Center for Nanoscale Systems (CNS), a member of the National Nanotechnology Coordinated Infrastructure Network (NNCI), which is supported by the National Science Foundation under NSF ECCS award no. 1541959. D.N.B., S.D., and the s-SNOM were supported by AFOSRFA9550-15-1-0478. D.N.B. is an investigator in Quantum Materials supported by the Gordon and Betty Moore Foundation's EPIQS Initiative through Grant GBMF4533.

Conflict of Interest

The authors declare no conflict of interest.

Keywords

2D materials, helium and neon ion beam fabrication, hexagonal boron nitride (h-BN), near-field imaging, photothermal effect

Received: January 7, 2018

Revised: March 9, 2018

Published online: April 24, 2018

- [1] A. K. Geim, I. V. Grigorieva, *Nature* **2013**, 499, 419.
- [2] D. N. Basov, M. M. Fogler, F. J. G. de Abajo, *Science* **2016**, 354, aag1992.
- [3] J. D. Caldwell, I. Vurgaftman, J. G. Tischler, O. J. Glembocki, J. C. Owrutsky, T. L. Reinecke, *Nat. Nanotechnol.* **2016**, 11, 9.
- [4] L. Wang, I. Meric, P. Y. Huang, Q. Gao, Y. Gao, H. Tran, T. Taniguchi, K. Watanabe, L. M. Campos, D. A. Muller, J. Guo, P. Kim, J. Hone, K. L. Shepard, C. R. Dean, *Science* **2013**, 342, 614.

- [5] S. M. Kim, A. Hsu, M. H. Park, S. H. Chae, S. J. Yun, J. S. Lee, D.-H. Cho, W. Fang, C. Lee, T. Palacios, M. Dresselhaus, K. K. Kim, Y. H. Lee, J. Kong, *Nat. Commun.* **2015**, *6*, 8662.
- [6] Z. Shi, X. Hong, H. A. Bechtel, B. Zeng, M. C. Martin, K. Watanabe, T. Taniguchi, Y.-R. Shen, F. Wang, *Nat. Photonics* **2015**, *9*, 515.
- [7] S. Dai, Z. Fei, Q. Ma, A. S. Rodin, M. Wagner, A. S. McLeod, M. K. Liu, W. Gannett, W. Regan, K. Watanabe, T. Taniguchi, M. Thiemens, G. Dominguez, A. H. C. Neto, A. Zettl, F. Keilmann, P. Jarillo-Herrero, M. M. Fogler, D. N. Basov, *Science* **2014**, *343*, 1125.
- [8] J. D. Caldwell, A. V. Kretinin, Y. Chen, V. Giannini, M. M. Fogler, Y. Francescato, C. T. Ellis, J. G. Tischler, C. R. Woods, A. J. Giles, M. Hong, K. Watanabe, T. Taniguchi, S. A. Maier, K. S. Novoselov, *Nat. Commun.* **2014**, *5*, 5221.
- [9] V. W. Brar, M. S. Jang, M. Sherrott, S. Kim, J. J. Lopez, L. B. Kim, M. Choi, H. Atwater, *Nano Lett.* **2014**, *14*, 3876.
- [10] S. Dai, Q. Ma, M. K. Liu, T. Andersen, Z. Fei, M. D. Goldflam, M. Wagner, K. Watanabe, T. Taniguchi, M. Thiemens, F. Keilmann, G. C. A. M. Janssen, S.-E. Zhu, P. Jarillo-Herrero, M. M. Fogler, D. N. Basov, *Nat. Nanotechnol.* **2015**, *10*, 682.
- [11] A. Kumar, T. Low, K. H. Fung, P. Avouris, N. X. Fang, *Nano Lett.* **2015**, *15*, 3172.
- [12] S. Dai, Q. Ma, T. Andersen, A. S. McLeod, Z. Fei, M. K. Liu, M. Wagner, K. Watanabe, T. Taniguchi, M. Thiemens, F. Keilmann, P. Jarillo-Herrero, M. M. Fogler, D. N. Basov, *Nat. Commun.* **2015**, *6*, 6963.
- [13] P. Li, M. Lewin, A. V. Kretinin, J. D. Caldwell, K. S. Novoselov, T. Taniguchi, K. Watanabe, F. Gaussmann, T. Taubner, *Nat. Commun.* **2015**, *6*, 7507.
- [14] A. J. Giles, S. Dai, O. J. Glembocki, A. V. Kretinin, Z. Sun, C. T. Ellis, J. G. Tischler, T. Taniguchi, K. Watanabe, M. M. Fogler, K. S. Novoselov, D. N. Basov, J. D. Caldwell, *Nano Lett.* **2016**, *16*, 3858.
- [15] X. Lin, Y. Yang, N. Rivera, J. J. López, Y. Shen, I. Kaminer, H. Chen, B. Zhang, J. D. Joannopoulos, M. Soljačić, *Proc. Natl. Acad. Sci. USA* **2017**, *114*, 6717.
- [16] N. Rivera, G. Rosolen, J. D. Joannopoulos, I. Kaminer, M. Soljačić, *Proc. Natl. Acad. Sci. USA* **2017**, 201713538.
- [17] G. Grosso, H. Moon, B. Lienhard, S. Ali, D. K. Efetov, M. M. Furchi, P. Jarillo-Herrero, M. J. Ford, I. Aharonovich, D. Englund, *Nat. Commun.* **2017**, *8*, 705.
- [18] A. W. Schell, T. T. Tran, H. Takashima, S. Takeuchi, I. Aharonovich, *APL Photonics* **2016**, *1*, 91302.
- [19] S. Biswas, C. S. Tiwary, S. Vinod, A. K. Kole, U. Chatterjee, P. Kumbhakar, P. M. Ajayan, *J. Phys. Chem. C* **2017**, *121*, 8060.
- [20] D. Winston, V. R. Manfrinato, S. M. Nicaise, L. L. Cheong, H. Duan, D. Ferranti, J. Marshman, S. McVey, L. Stern, J. Notte, K. K. Berggren, *Nano Lett.* **2011**, *11*, 4343.
- [21] F. H. M. Rahman, S. McVey, L. Farkas, J. A. Notte, S. Tan, R. H. Livengood, *Scanning* **2012**, *34*, 129.
- [22] J. J. Lopez, F. Greer, J. R. Greer, *J. Appl. Phys.* **2010**, *107*, 104326.
- [23] G. Nanda, S. Goswami, K. Watanabe, T. Taniguchi, P. F. A. Alkemade, *Nano Lett.* **2015**, *15*, 4006.
- [24] D. C. Bell, M. C. Lemme, L. A. Stern, J. R. Williams, C. M. Marcus, *Nanotechnology* **2009**, *20*, 455301.
- [25] M. C. Lemme, D. C. Bell, J. R. Williams, L. A. Stern, B. W. H. Baugher, P. Jarillo-Herrero, C. M. Marcus, *ACS Nano* **2009**, *3*, 2674.
- [26] A. N. Abbas, G. Liu, B. Liu, L. Zhang, H. Liu, D. Ohlberg, W. Wu, C. Zhou, *ACS Nano* **2014**, *8*, 1538.
- [27] S. Hang, Z. Moktadir, H. Mizuta, *Carbon* **2014**, *72*, 233.
- [28] D. S. Fox, Y. Zhou, P. Maguire, A. O'Neill, C. Ó'Coileáin, R. Gatensby, A. M. Glushenkov, T. Tao, G. S. Duesberg, I. V. Shvets, M. Abid, M. Abid, H.-C. Wu, Y. Chen, J. N. Coleman, J. F. Donegan, H. Zhang, *Nano Lett.* **2015**, *15*, 5307.
- [29] P. Maguire, D. S. Fox, Y. Zhou, Q. Wang, M. O'Brien, J. Jadwiszczak, J. McManus, N. McEvoy, G. S. Duesberg, H. Zhang, *arXiv:condmat/1707.08893v2* **2017**.
- [30] F. Lu, M. Jin, M. A. Belkin, *Nat. Photonics* **2014**, *8*, 307.
- [31] Z. Fei, A. S. Rodin, G. O. Andreev, W. Bao, A. S. McLeod, M. Wagner, L. M. Zhang, Z. Zhao, M. Thiemens, G. Dominguez, M. M. Fogler, A. H. C. Neto, C. N. Lau, F. Keilmann, D. N. Basov, *Nature* **2012**, *487*, 82.
- [32] J. Chen, M. Badioli, P. Alonso-González, S. Thongrattanasiri, F. Huth, J. Osmond, M. Spasenovi, A. Centeno, A. Pesquera, P. Godignon, A. Zurutuza Elorza, N. Camara, F. J. G. de Abajo, R. Hillenbrand, F. H. L. Koppens, *Nature* **2012**, *487*, 77.
- [33] K. S. Novoselov, D. Jiang, F. Schedin, T. J. Booth, V. V. Khotkevich, S. V. Morozov, A. K. Geim, *Proc. Natl. Acad. Sci. USA* **2005**, *102*, 10451.
- [34] R. Siegle, G. C. Weatherly, H. K. Haugen, D. J. Lockwood, L. M. Howe, *Appl. Phys. Lett.* **1995**, *66*, 1319.
- [35] S. Tan, R. Livengood, P. Hack, R. Hallstein, D. Shima, J. Notte, S. McVey, *J. Vac. Sci. Technol., B: Nanotechnol. Microelectron.: Mater. Process., Meas., Phenom.* **2011**, *29*, 06F604.
- [36] R. S. Averbach, M. Ghaly, *J. Appl. Phys.* **1994**, *76*, 3908.
- [37] J. F. Ziegler, M. D. Ziegler, J. P. Biersack, *Nucl. Instrum. Methods Phys. Res., Sect. B* **2010**, *268*, 1818.
- [38] L. A. Giannuzzi, *Introduction to Focused Ion Beams: Instrumentation, Theory, Techniques and Practice*, Springer Science & Business Media, New York **2006**.
- [39] M. G. Stanford, B. B. Lewis, K. Mahady, J. D. Fowlkes, P. D. Rack, *J. Vac. Sci. Technol., B: Nanotechnol. Microelectron. Mater.: Process., Meas., Phenom.* **2017**, *35*, 30802.
- [40] I. Utke, S. Moshkalev, P. Russell, *Nanofabrication Using Focused Ion and Electron Beams: Principles and Applications*, Oxford University Press, Oxford **2012**.
- [41] C. A. Volkert, A. M. Minor, *MRS Bull.* **2007**, *32*, 389.
- [42] O. Lehtinen, J. Kotakoski, A. V. Krasheninnikov, A. Tolvanen, K. Nordlund, J. Keinonen, *Phys. Rev. B* **2010**, *81*, 153401.
- [43] *J. Vac. Sci. Technol., B: Nanotechnol. Microelectron. Mater.: Process., Meas., Phenom.* **2010**, *28*, C6F15.
- [44] R. J. Nemanich, S. A. Solin, R. M. Martin, *Phys. Rev. B* **1981**, *23*, 6348.
- [45] S. Reich, A. C. Ferrari, R. Arenal, A. Loiseau, I. Bello, J. Robertson, *Phys. Rev. B* **2005**, *71*, 205201.
- [46] R. V. Gorbachev, I. Riaz, R. R. Nair, R. Jalil, L. Britnell, B. D. Belle, E. W. Hill, K. S. Novoselov, K. Watanabe, T. Taniguchi, A. K. Geim, P. Blake, *Small* **2011**, *7*, 465.
- [47] G. H. Han, J. A. Rodríguez-Manzo, C.-W. Lee, N. J. Kybert, M. B. Lerner, Z. J. Qi, E. N. Dattoli, A. M. Rappe, M. Drndic, A. T. C. Johnson, *ACS Nano* **2013**, *7*, 10129.
- [48] G. Lu, T. Wu, Q. Yuan, H. Wang, H. Wang, F. Ding, X. Xie, M. Jiang, *Nat. Commun.* **2015**, *6*, 6160.
- [49] P. G. Spizzirri, J.-H. Fang, S. Rubanov, E. Gauja, S. Praver, *arXiv:condmat/1002.2692v1* **2010**.
- [50] A. Ambrosio, L. Jauregui, S. Dai, K. Chaudhary, M. Tamagnone, M. M. Fogler, P. D. Basov, F. Capasso, P. Kim, W. L. Wilson, *ACS Nano* **2017**, *11*, 8741.
- [51] C. Martinet, R. a. B. Devine, *J. Appl. Phys.* **1995**, *77*, 4343.
- [52] A. C. Ferrari, J. C. Meyer, V. Scardaci, C. Casiraghi, M. Lazzeri, F. Mauri, S. Piscanec, D. Jiang, K. S. Novoselov, S. Roth, A. K. Geim, *Phys. Rev. Lett.* **2006**, *97*, 187401.
- [53] Y. Hao, Y. Wang, L. Wang, Z. Ni, Z. Wang, R. Wang, C. K. Koo, Z. Shen, J. T. L. Thong, *Small* **2010**, *6*, 195.
- [54] B. Yates, M. J. Overy, O. Pirgon, *Philos. Mag.* **1975**, *32*, 847.
- [55] I. M. Lifshits, *Zh. Eksp. Teor. Fiz.* **1952**, *22*, 475.
- [56] G. L. Belenkii, E. Y. Salaev, R. A. Suleimanov, N. A. Abdullaev, V. Y. Shteinshraiber, *Solid State Commun.* **1985**, *53*, 967.
- [57] P. Li, I. Dolado, F. J. Alfaro-Mozaz, F. Casanova, L. E. Hueso, S. Liu, J. H. Edgar, A. Y. Nikitin, S. Vélez, R. Hillenbrand, *Science* **2018**, *359*, 892.
- [58] K. S. Novoselov, A. Mishchenko, A. Carvalho, A. H. C. Neto, *Science* **2016**, *353*, aac9439.
- [59] P. Ajayan, P. Kim, K. Banerjee, *Phys. Today* **2016**, *69*, 39.
- [60] I. Horcas, R. Fernández, J. M. Gómez-Rodríguez, J. Colchero, J. Gómez-Herrero, A. M. Baro, *Rev. Sci. Instrum.* **2007**, *78*, 13705.